Conference on Modelling Fluid Flow (CMFF'25)
The 19th International Conference on Fluid Flow Technologies
Budapest, Hungary, August 26-August 29, 2025

Development of a Cerebral Peripheral Vasculature Model for Quantitative Assessment of Collateral Blood Flow using SPECT and 4D Flow MRI

To Chi Hang[1], Shigeki Yamada[2], Marie Oshima[3]

[1] Corresponding Author. Graduate School of Engineering, Department of Mechanical Engineering, University of Tokyo. 7-3-1 Hongo, Bunkyo-ku, Tokyo 113-8654, Japan. Tel.: +81 80 4476 3065, E-mail: to-chi-hang524@g.ecc.u-tokyo.ac.jp
[2] Graduate School of Medical Sciences, Department of Neurosurgery, Nagoya City University Graduate School of Medical Sciences. E-mail: shigekiyamada393@gmail.com
[3] Institute of Industrial Science / Graduate School of Interdisciplinary Information Studies, The University of Tokyo. E-mail: marie@iis.u-tokyo.ac.jp

ABSTRACT

Collateral blood flow redistribution is crucial in ischemic stroke recovery, yet the role of leptomeningeal anastomoses (LMAs) remains poorly characterized. Current computational models lack representation of patient-specific redistribution under varying ischemic conditions. As such, this study investigates LMA functionality using patient-specific data. A 0D peripheral artery model, informed by anatomical measurements and Circle of Willis (CoW) vessel radii from medical images, is constructed using a stochastic sampling approach. To identify LMA configurations that align with measured data, island Genetic Algorithm (iGA) optimises LMA configuration by minimizing residuals between computed and measured perfusion flow rates from Single Photon Emission Computed Tomography (SPECT), with 4D flow MRI (magnetic resonance imaging) data serving as inlet flow rates. Case studies of two patients with varying degrees and locations of internal carotid artery stenosis reveal redistribution patterns consistent with physiological observations, including anterior-directed perfusion and inter-hemispheric redistribution. Topology analysis reveals a trade-off between LMA radius and pressure difference, with larger radii forming between arteries at lower bifurcation depths, enhancing flow rate despite diminishing pressure differences. By leveraging measurement techniques, this study offers new insights into patient-specific LMA morphology, with potential applications in refining more detailed vascular models for clinical and research use.

Keywords: cerebrovascular haemodynamics, collateral blood flow, genetic algorithm, leptomeningeal anastomosis, stochastic vasculature generation

NOMENCLATURE

G	$[\frac{\text{mL/s}}{\text{mmHg}}]$	conductance
H	$[-]$	number of vascular regions
J	$[-]$	cost function
L	$[mm]$	length
Q	$[mL/s]$	flow rate
R	$[\frac{mmHg}{\text{mL/s}}]$	resistance
d	$[-]$	bifurcation depth
p	$[mmHg]$	pressure
r	$[mm]$	radius
μ	$[Pa \cdot s]$	viscosity
τ	$[mmHg]$	fluid shear stress
$\lambda_{l/r}$	$[-]$	length-to-radius ratio
$\mathcal{N}$	$[-]$	node
R_{eff}	$[\frac{mmHg}{\text{mL/s}}]$	effective resistance

Subscripts and Superscripts

Co	computed
Sp	SPECT
int	internal

1. INTRODUCTION

Collateral blood flow plays a critical role in maintaining cerebral perfusion during arterial occlusions [1, 2], yet its assessment remains a challenge in both clinical and computational settings [3]. Traditional imaging techniques such as 4D Flow MRI and SPECT provide valuable insights into cerebral haemodynamics but are often limited by spatial resolution and qualitative interpretation, particularly in the context of small collateral vessels such as LMAs. These vessels, typically less than 0.3 mm in diameter [4], contribute to blood flow redistribution between vascular territories, yet their functional significance and flow dynamics remain difficult to quantify directly from imaging data.

Computational fluid dynamics (CFD) offers a complementary approach by enabling quantitative assessment of collateral circulation. Unlike imaging-based methods, CFD allows for controlled parameter variation, facilitating sensitivity analyses and predictive modelling of haemodynamic changes under different physiological and pathological conditions. However, conventional CFD methods, including 3D and even 1D simulations, are computationally intensive and impractical for large-scale uncertainty analyses or real-time clinical application [5]. As a result, 0D modelling has emerged as a viable alternative, offering an efficient means to simulate cerebral blood flow while preserving essential flow redistribution characteristics [6].

Despite its advantages, traditional 0D models often simplify vascular territories as isolated compartments, with collateral connections represented by literature-derived resistances rather than patient-specific data [7]. This simplification limits the ability to investigate collateral recruitment dynamics in an anatomically realistic manner.

To improve the physiological accuracy of flow simulations while maintaining computational efficiency, a more refined 0D modelling framework is needed—particularly for representing the peripheral vascular network. A key challenge in this approach is the scarcity of patient-specific vascular data, as direct segmentation of small vessels like LMAs is often impractical in clinical settings. To address this, synthetic vasculature generation offers a viable solution, enabling the creation of vascular networks that reflect anatomical variability with minimal input data [8].

This study presents a 0D modelling framework that integrates flow rate measurements with synthetic vascular network generation to enhance collateral circulation assessment. By minimizing reliance on explicit vascular segmentation, this approach enables the simulation of patient-specific flow dynamics without requiring detailed anatomical reconstructions. The model is designed to be computationally efficient via vasculature lumping to a certain extent without the loss of essential structural information, allowing for rapid simulation of collateral flow scenarios under varying conditions. Through this framework, it is hoped that it would advance the practical application of CFD in cerebrovascular research, bridging the gap between imaging-based assessments and predictive haemodynamic modelling.

2. METHOD

This study aims to create an explicit and computationally efficient vascular network model that includes LMAs, to study how they redistribute blood flow. Synthetic vascular trees are generated using anatomical data, such as bifurcation patterns and artery sizes from cadaver studies, with a stochastic approach to model variability in the generated structures. Six vascular trees, one for each vascular region, are selected for fluid simulations, with patient-specific 4D flow MRI data providing boundary conditions to reflect real physiological conditions. LMAs are then positioned to connect these trees, mimicking the restoration of blood flow in response to blockages. The placement of LMAs is optimized using iGA, which minimizes the difference between simulated flow rates and those measured by SPECT. This process is repeated over multiple iterations to generate different combinations of vascular trees and LMA configurations, ensuring that the best arrangements are found while adhering to physiological constraints. The overall goal is to identify the LMA placements under a range of potential patient-specific peripheral vasculature that recreate the blood flow redistribution shown in measured data.

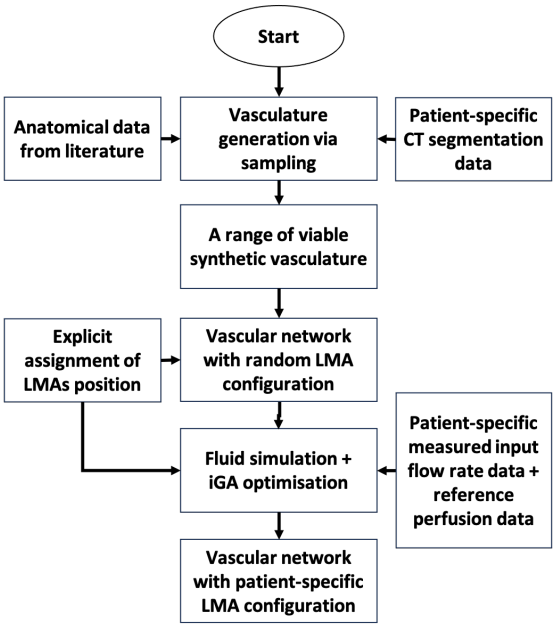

Figure 1. Flowchart depicting the process of deducing patient-specific LMA placement for blood flow redistribution using synthetic vascular trees and patient-specific flow rate data.

2.1. Data Acquisition

To generate a synthetic vasculature model for each of the six vascular regions, only the radii of the six efferent arteries of the CoW —the anterior, middle, and posterior cerebral arteries (ACA, MCA, PCA) on both hemispheres—are required. This differs from traditional methods that rely on imaging beyond the CoW, reducing the dependency on high-resolution medical images. Any loss in model resolution is addressed through uncertainty analysis, considering all plausible vasculature based on available data.

The inlet radii of the peripheral vasculature were derived from segmented CT images, with vessel centrelines extracted and smoothed using software "V-Modeler" [9]. The average radii along these centrelines were computed for use as model inlets.

Regional perfusion distributions were derived from SPECT imaging [10], with patient-specific vascular regions identified through shape registration between SPECT images and an atlas vascular region map. Voxel intensity values were then used to estimate regional flow rates. Since total cerebral blood flow (CBF) measured by SPECT and 4D Flow MRI differs, SPECT-derived flow rates were adjusted to match total CBF, which was determined by summing the MRI-measured flow rates of the internal carotid and basilar arteries, as 4D Flow MRI provides the most accurate measurements in larger arteries. Meanwhile, flow entering the peripheral regions through the six efferent arteries of the CoW was obtained from 4D Flow MRI. Similar to the SPECT-derived values, the outflow rates at the CoW were scaled based on inlet MRI data.

2.2. Sampling and Generation of Vascular Tree Models

To ensure anatomical accuracy, the vascular tree model is constructed based on observed anatomical structures, referencing Perlmutter and Rhoton [11], Gibo et al. [12], and Zeal and Rhoton [13]. Across all six vascular regions, the vasculature follows a consistent bifurcation pattern: perforating trunks traverse the brain, cortical branches extend perpendicularly, and perfusion arterioles supply the cortex. The model is represented as a graph, with nodes corresponding to bifurcation points and edges representing vessel segments, starting with an inlet node at the CoW, marking the entry to the peripheral vascular region. Given a list of candidate cortical branches from literature, each branch is probabilistically determined based on observed frequencies. If fenestration (multiple copies of the same branch) is observed, the number of copies is sampled from a Poisson distribution, and the branch radius is sampled from measured data ranges. After the first cortical branch radius is assigned, the subsequent perforating trunk segment radius is calculated using Murray's law, which states that the cube of the parent vessel radius equals the sum of the cubes of the daughter vessel radii. This process repeats for all candidate branches in the vascular region. If at any point the perforating trunk radius reduces to zero due to sampling variability, the entire process restarts from the first cortical branch candidate.

Perfusion arterioles extend from each cortical branch, assuming equal bifurcation at each level, until reaching the cut-off radius of 0.025 mm. Given depth d as the number of bifurcations from the cortical branch, the arteriole radius at depth d is given by Eq. (1):

$$r_d = r_0 \cdot \left(\frac{1}{2^{1/3}}\right)^d \tag{1}$$

Assuming a constant length-to-radius ratio $\lambda_{l/r}$, the vessel resistance is computed using Eq. (2), based on Poiseuille's law, which is derived from the Navier-Stokes equation under the assumptions of steady, incompressible flow in a cylindrical vessel:

$$R = \frac{8\mu \cdot l_{\text{lma}}}{\pi r^4} \tag{2}$$

Given the homogeneous structure of perfusion arterioles, the total resistance of the arteriole tree at depth d is obtained by series-parallel resistance aggregation, as described by Eq. (3):

$$R_{\text{eff}} = \sum_{k=0}^{d} \frac{R_k}{2^k} \tag{3}$$

Where the radius and resistance at each depth k can be calculated using Eq. (1) and Eq. (2). This reduces the number of nodes from $2^d + 1$ to just 2, significantly improving computational speed for LMA optimization, which is essential for the large number of fluid simulations required.

In the context of this model, an LMA's location is fully defined by the two arterioles it connects, characterized by three parameters: vascular region, cortical branch, and bifurcation depth. To incorporate an LMA, a new node representing its connection point is added between the cortical branch bifurcation and the distal end of its arteriole tree. The arteriole tree's resistance is split into upstream and downstream portions, ensuring efficient flow traversal while maintaining computational efficiency.

Figure 2 presents a schematic representation of a vascular tree, illustrating the node placements for LMA connections. Nodes represent bifurcation points, and edges correspond to blood vessel segments. Arrows indicates the direction of blood flow from inlet to outlet. Red dashed lines depict LMA connections to another vascular region.

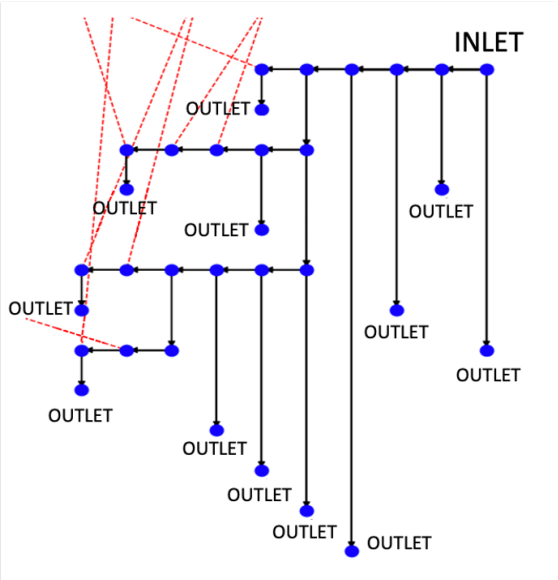

Figure 2. Schematic representation of a vascular tree

2.3. Fluid simulation

Blood flow in this study is simulated using a 0D haemodynamic model based on steady-state flow assumptions, where vessel segments are treated as resistive elements. Blood is modeled as an incompressible Newtonian fluid with a viscosity of 4.7 mPa·s.

The vascular network consists of six primary inlet nodes, corresponding to arterial branches from the CoW, and multiple outlet nodes representing cortical branch terminations. Flow rate boundary conditions are imposed at the inlet nodes, derived from patient-specific 4D Flow MRI data. At the outlet nodes, a fixed pressure value of 50 mmHg is assigned, which approximates typical pial arteriole pressures ($\sim 50\,\mu$m in diameter). Although physiological variability exists in outlet pressures, this fixed value serves as a practical approximation. Future iterations of the model could incorporate a venous compartment to dynamically compute outlet pressures, eliminating the need for fixed boundary conditions.

Pressure distribution within the vascular network is computed using a conductance-based approach, where each vessel segment is characterized by the inverse of its resistance. The pressure at each node is determined by solving the conservation of momentum equation, Eq. (4):

$$G_{ij}(p_i - p_j) = Q_{ij}, \tag{4}$$

where G_{ij} represents the conductance between nodes i and j, p_i and p_j denote the pressure at nodes i and j, respectively, and Q_{ij} represents the flow rate between the two nodes.

To satisfy mass conservation, the sum of all incoming and outgoing flows at each internal node must be zero. Mathematically, this is presented as Eq. (5).

$$\sum_j Q_{ij} = 0, \quad \forall i \in \mathcal{N}_{\text{int}}, \tag{5}$$

where $\mathcal{N}_{\text{int}}$ denotes the set of all internal nodes, excluding inlets and outlets.

Boundary conditions are imposed such that a prescribed net inflow $Q_i \neq 0$ is applied at inlet nodes, while outlet nodes have fixed pressure values. This formulation results in a sparse linear system for the unknown nodal pressures. To efficiently solve this system, the model employs the Compressed Sparse Column (CSC) format, which minimizes memory usage and computational cost. A direct solver optimized for sparse matrices is used, ensuring stability and efficiency in handling large vascular networks. Once the pressure field is computed, the flow rates through each vessel segment are determined based on Eq. (4). The total distal flow rate for each vascular region is obtained by summing the contributions from all outlet nodes within that region. The overall computational framework allows for rapid analysis, with the average runtime for solving the CSC system and determining node pressures being approximately 0.02 seconds.

2.4. Obtaining patient-specific LMA configuration

This section details the optimisation process to identify the LMA configurations that replicate observed flow redistribution in cerebral vasculature. Given the measured 4D flow MRI flow rates at inlets, the goal is to find the LMA configuration that produces regional distal flow rates that match the measured SPECT flow rates in each region. The distal flow rate $Q_{\text{com},h}$ for each vascular region h is determined by summing the flow rates at all outlet nodes within that region.

Given the discrete nature of the problem, where LMA placement is represented by a set of discrete decisions rather than continuous parameters, the problem is classified as a discrete combinatorial optimisation problem. The search space grows exponentially with the number of candidate locations, making an exhaustive search computationally infeasible. Therefore, an iGA was chosen to perform the optimisation. LMA configuration, encoded as a set of potential LMA locations, serves as the decision variable. Meanwhile, the cost function J, shown in Eq. 6, is defined as the RMS error between computed and observed flow rates.

$$J = \sqrt{\frac{1}{H}\sum_{\text{h}=1}^{H}(Q_{\text{Co,h}} - Q_{\text{Sp,h}})^2} \tag{6}$$

The constraints on formation of solution are as follows: (1) Only inter-vascular-region LMAs are considered, with connections defined based on previous studies. These include connections from the ACA to MCA superior trunk branches, PCA to MCA inferior trunk branches, ACA to PCA across hemispheres, and left ACA to right ACA. (2) The difference in radii at the connected arterioles is constrained to a maximum of 0.1 mm. This ensures that the assumption of arteriogenesis, by which LMAs form, requires connections between similarly sized arterioles. (3) Only arterioles that are at least three bifurcations downstream from the cortical branch are considered for LMA connections. This reflects the fact that LMAs most commonly form on the meningeal surface rather than within the cortical network. (4) The maximum number of LMAs allowed in any given configuration is set to 400, a value sufficiently high for the cases tested. It should be noted that, in practice, the number of LMAs in optimized configurations typically remains well below this upper bound.

Shear stress is a crucial factor in arteriogenesis, as the mechanical forces induced by blood flow through vessels promote endothelial activation and subsequent vessel remodelling [14]. In the context of the optimisation, a shear stress constraint is imposed

to prevent the formation of inefficient LMAs. The fluid shear stress (FSS) for a blood vessel, assuming Poiseuille flow and neglecting tortuosity, is given by Eq. 7.

$$\tau = \frac{4\mu Q}{\pi r^3} \tag{7}$$

The FSS constraint enforces that each LMA must maintain a minimum shear stress value for the connection to be valid in the solution. The minimum FSS limit is set at 2.5 Pascals, referencing the lower end of the range measured in [15].

The inherent uncertainty in SPECT measurements is assumed conservatively to be 10% [6]. Given this assumption, a solution is considered satisfactory if the residuals for each vascular region—i.e., the difference between the SPECT-derived and computed distal flow rates in the region—falls within 10% of the scaled SPECT flow rate. This ensures that the maximum discrepancy between the two values remains within the uncertainty range, effectively allowing the computed flow rate to be considered a match to the SPECT flow rate once it falls within this threshold. Mathematically, this can be expressed as Eq. 8.

$$\left|Q_{\mathrm{Co,\,h}} - Q_{\mathrm{Sp,h}}\right| \leq 0.05 \cdot Q_{\mathrm{Sp},h}, \quad \forall h \in \{1, 2, \ldots, H\} \tag{8}$$

At the start of the optimisation process, a set of 6 vascular tree models is chosen from a pre-generated pool of models. A population is initialised through random generation of valid solutions. To enhance the diversity of the search space and avoid premature convergence, the population is divided into multiple subpopulations, or "islands," that evolve independently. Regular migration between islands ensures the exchange of promising solutions. Once the initial population is set, each solution is evaluated by adding the encoded LMAs to the vasculature and performing fluid simulations. The cost of each solution is determined by comparing the computed distal flow rates with the target flow rates from SPECT data.

In the next phase, the rank-based exponential selection algorithm is applied to promote solutions with lower costs. Solutions are ranked based on their cost, and the probability of selection for reproduction is higher for solutions with better performance. After selection, crossover, mutation, and solution length adjustment operations are applied to generate new solutions for the next generation. Crossover involves combining parts of two parent solutions, while mutation introduces small random changes to the solutions. Length adjustment modifies the number of LMAs in a solution to explore different regions of the solution space. Solutions of the next generation is then evaluated, and the iterative process continues until a satisfactory solution is found, or when the maximum number of allowed generations has elapsed, at which point no successful LMA configuration is found for the set of vascular tree models. The models will be returned to the selection pool to be selected again.

3. RESULTS

Two patient cases are examined to illustrate the model's practical application: CEA12, a 68-year-old male with bilateral ICA stenosis (63% left, 65% right), and CEA13, a 72-year-old male with severe right ICA stenosis (91%). For each case, 2,000 vascular tree models were generated per vascular region, and 250 optimized peripheral vasculature-LMA configuration pairs were collected using a stochastic selection methodology. The time required to obtain one optimized LMA configuration varied, with CEA13 taking 257.93 ± 106.53 seconds and CEA12 taking 169.87 ± 118.20 seconds, both of which are acceptable in the scope of this study.

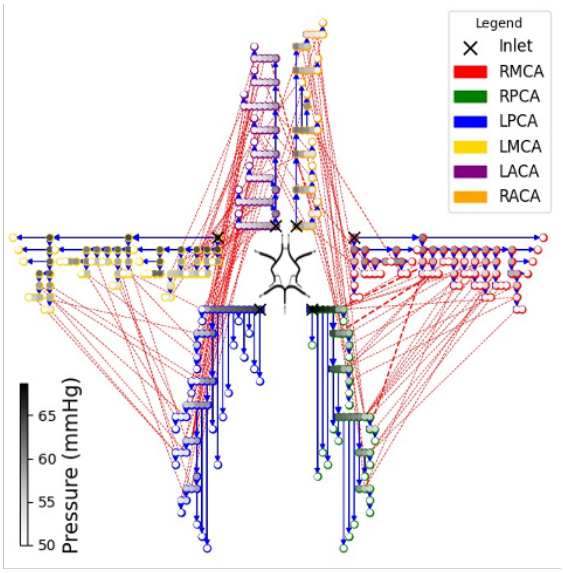

Figure 3. Representative model for case CEA12. Flow direction is indicated by blue arrows, and nodal pressure is visualized using in greyscale.

Figure 3 and 4 present schematic graph plots for cases CEA12 and CEA13, with one peripheral vasculature model from each case selected as a representative sample. In CEA13, due to stenosis on the right-hand side, the pressure in the left hemisphere is elevated compared to the right. LMAs are highlighted in red, with line thickness representing conductance of LMA. In CEA13, a greater number of high-conductance LMAs are observed between the left and right anterior cerebral arteries (ACA), reflecting an increased reliance on inter-hemispheric collateral flow. This recruitment of LMAs is driven by the pressure gradient across hemispheres, created by the single-sided stenosis in case CEA13. The pressure in the right PCA of case CEA13 is also higher, reflecting the reliance on perfusion via the healthy BA instead of the stenosed right ICA.

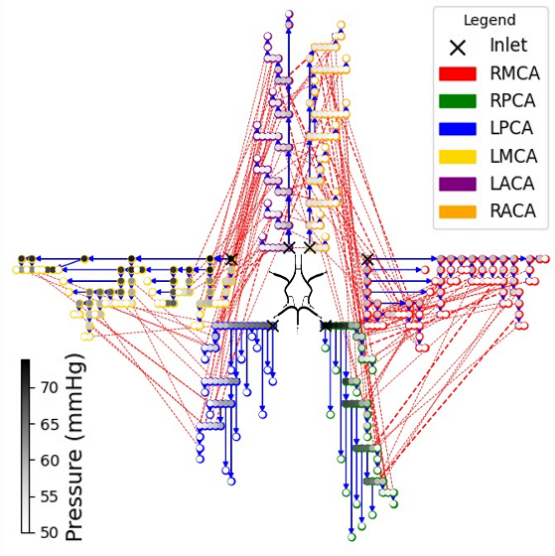

Figure 4. Representative model for case CEA13, in the same format as that for case CEA12.

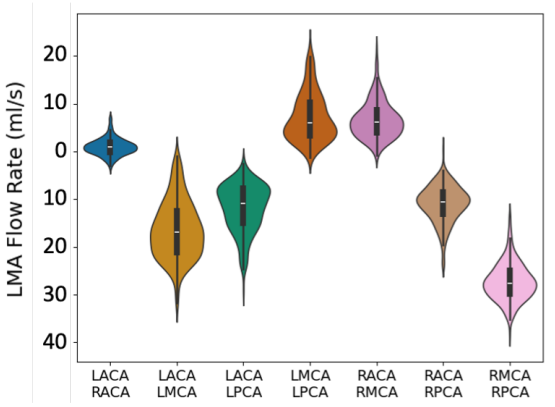

Figure 5. Redistribution of flow rates through each collateral pathway for case CEA12

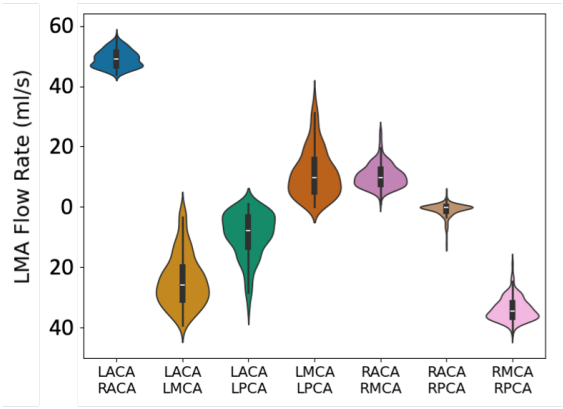

Figure 6. Redistribution of flow rates through each collateral pathway for case CEA13

Figure 5 and 6 present violin plots illustrating the redistribution of flow rates through each collateral pathway, with its pattern differing between cases. Flow rates positioned below zero indicate redistribution from the second vascular region in the label to the first, whereas positive values indicate flow in the opposite direction. In CEA13, inter-hemispheric flow accounts for 11.5% of the total cerebral blood flow, whereas in CEA12, it is significantly lower at 0.23%. Significant flow from right PCA to right MCA aligns with expectation of collateral flow from posterior to anterior circulation. The observed range of redistribution is a result of variations in the vascular tree structure, which alter the relative pressure distribution between regions, in turn leading to differences in LMA recruitment and adaptation. Notably, changes in the vascular structure do not result in unrealistic or excessive variability in flow redistribution patterns. The distribution remains unimodal, as confirmed by Hartigan's Dip Test, indicating a stable adaptation mechanism despite differences in vascular topology.

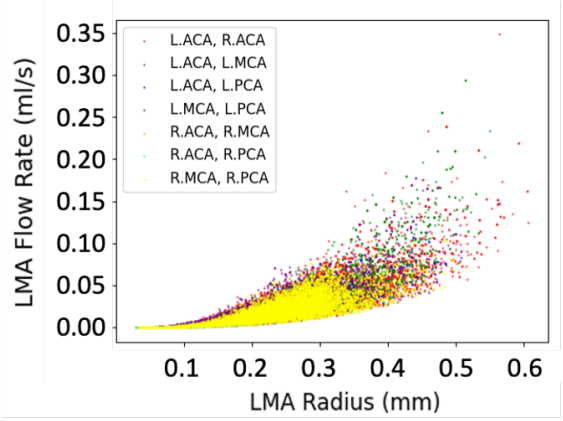

Figure 7. Flow rate vs. radius of LMA, CEA13

Figure 7 presents a flow rate versus radius plot for CEA13, illustrating the redistributed flow rate of each individual LMA across 250 optimized configurations as a function of its respective radius. Each dot represents a single LMA, with the colour scale indicating the associated collateral pathway. The fan-shaped void near the $y = 0$ line suggests that FSS constraint is functioning as intended, as LMAs with a high radius but low flow rate are correctly suppressed, with larger radius leading to higher flow rates in general. This confirms that the fluid simulation operates as expected.

Figure 8 presents a plot of pressure difference versus radius for CEA13, illustrating the pressure difference between the two arterioles connected by each LMA, plotted against their respective radii across all 250 optimized configurations. The results reveal a trade-off between radius and pressure difference. Due to the physiologically-based constraint that the radius difference between the two arterioles connected by an LMA must remain under 0.1 mm, LMAs with larger radii typically form between arteries at lower bifurcation depths, which are located

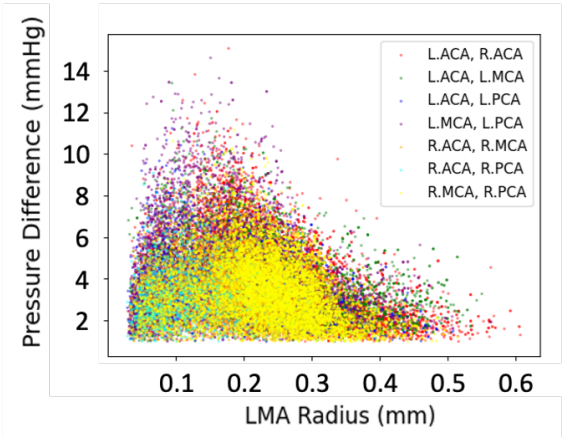

Figure 8. Pressure difference across LMA vs. their respective radii, CEA13

more proximally in the vascular tree. As pressure dissipates downstream, arteries at similar depths exhibit smaller pressure differences compared to arteries at significantly different depths, where the upstream end has a much higher pressure relative to the downstream end. In such cases where the pressure difference is favourable for more efficient redistribution, the smaller radius of the downstream arteriole limits the LMA's overall radius.

While the maximum pressure difference occurs around a radius of 0.2 mm, the maximum flow rate continues to increase with radius, despite lower pressure differences. This behaviour aligns with Poiseuille's equation, which states that flow rate is proportional to the pressure difference but inversely scales with the cube of the radius. Consequently, radius exerts a dominant influence over flow rate, reinforcing that the model accurately reflects the expected behaviour of LMAs from a fluid dynamics perspective.

Finally, it is important to note that the mean LMA radius for each case was found to be 0.212 ± 0.0927 mm for CEA13 and 0.169 ± 0.0857 mm for CEA12. These values are consistent with existing literature, with CEA12 showing a smaller LMA radius compared to CEA13. This difference is likely due to CEA12 needing to prioritize the pressure difference across LMAs by connecting upstream arterioles to downstream ones. Since the inherent pressure difference between vascular regions—and between arterioles at the upstream end of the cortical branch trees—is relatively small, CEA12 compensates by relying on the pressure difference generated by the depth disparity between these arteries.

4. DISCUSSION

This study employs a 0D model due to its suitability for capturing global flow distribution in a simplified and computationally efficient manner. The decision to explicitly compute the radius of each blood vessel segment, and directly derive resistance from anatomical parameters, eliminates the need for empirical tuning. This approach makes the model ideal for steady-state analysis of systemic haemodynamics, as outlined by Shi et al. [5]. It also retains flexibility and simplicity when modelling arterial flow redistribution.

One limitation of this study is the lack of capillary-level analysis, which is essential for understanding microvascular perfusion. Additionally, the model is relatively coarse, considering only six vascular regions, which introduces significant uncertainty in the redistribution of flow values. The study, however, lays the foundation for future research that will incorporate larger datasets and finer perfusion partitioning at the cortical region level. This would be particularly beneficial given the rapid advancements in imaging techniques that are less invasive, more affordable, and increasingly applicable in clinical settings [16]. The increased precision in these imaging techniques would reduce uncertainty in flow redistribution calculations. As more regions are considered, the model would be required to satisfy more complex redistribution conditions. While this adds difficulty, it ultimately leads to more precise and refined insights into haemodynamic behaviour.

Here, the model's scalability should be noted, as it can easily adapt to perfusion data of different precision levels by adjusting the partitioning of regions of interest. Currently, the model is based on just six vascular regions, but it can be extended down to the level of individual cortical branches. This flexibility will allow for the integration of more detailed pial perfusion data, which will contribute to advancing the understanding of local blood flow dynamics. Ultimately, this will enable the development of more accurate, patient-specific predictive models for stroke management.

Validation of both vasculature structure and LMA topology remains a challenging task. It is hoped that future advancements in imaging techniques will provide more quantitative data for validation, allowing for more robust assessments of the model's accuracy. The study is currently advancing in the direction of performing comparative analyses with a broader range of patient cases. This work aims to deepen the understanding of the relationship between variations in both LMA topology and overall vasculature network structure, particularly in response to changes in pressure environments, physiological conditions, and distal perfusion demands.

5. CONCLUSION

A 0D modelling framework that integrates synthetic vascular network generation with flow rate measurements to enhance the assessment of cerebral collateral circulation was introduced. This approach enables patient-specific simulations without requiring detailed vascular segmentation whilst taking in account peripheral collateral network, addressing

key limitations in traditional peripheral vasculature models, thus representing a step toward bridging the gap between imaging-based assessments and predictive haemodynamic modelling, offering a practical approach for investigating cerebrovascular haemodynamics in both research and clinical settings. Future work will focus on validating LMA topology and model performance, increasing model granularity, and expanding the analysis to a broader range of patient cases.

6. ACKNOWLEDGEMENTS

This work was supported by the Fugaku project titled *Development of human digital twins for cerebral circulation using Fugaku*, carried out at the RIKEN Center for Computational Science (Project ID: **hp240220**); as well as by the JSPS KAKENHI grant *Development of an analysis system of systemic-cerebral circulatory metabolism for stroke risk prediction* (Project ID: **22H00190**).

REFERENCES

[1] Odano, I., Tsuchiya, T., Nishihara, M., Sakai, K., Abe, H., and Tanaka, R., 1993, "Regional Cerebral Blood Flow Measured With N-Isopropyl-p- [123I] Iodoamphetamine and Its Redistribution in Ischemic Cerebrovascular Disease", *Stroke*, Vol. 24, pp. 1167–1172.

[2] Shuaib, A., Butcher, K., Mohammad, A., Saqqur, M., and Liebeskind, D., 2011, "Collateral blood vessels in acute ischaemic stroke: a potential therapeutic target", *The Lancet Neurology*, Vol. 10, pp. 909–921.

[3] Brozici, M., van der Zwan, A., and Hillen, B., 2003, "Anatomy and functionality of leptomeningeal anastomoses: a review", *Stroke*, Vol. 34 (11), pp. 2750–2762.

[4] Vander Eecken, H. M., and Adams, R. D., 1953, "The anatomy and functional significance of the meningeal arterial anastomoses of the human brain", *J Neuropathol Exp Neurol*, Vol. 12 (2), pp. 132–157.

[5] Shi, Y., Lawford, P., and Hose, R., 2011, "Review of zero-D and 1-D models of blood flow in the cardiovascular system", *Biomed Eng Online*, Vol. 10, p. 33.

[6] Zhang, H., Fujiwara, N., Kobayashi, M., Yamada, S., Liang, F., Takagi, S., and Oshima, M., 2016, "Development of a Numerical Method for Patient-Specific Cerebral Circulation Using 1D-0D Simulation of the Entire Cardiovascular System with SPECT Data", *Annals of biomedical engineering*, Vol. 44 (8), pp. 2351–2363.

[7] Ryu, J., Hu, X., and Shadden, S. C., 2015, "A Coupled Lumped-Parameter and Distributed Network Model for Cerebral Pulse-Wave Hemodynamics", *Journal of Biomechanical Engineering*, Vol. 137 (10), p. 101009.

[8] Ii, S., Kitade, H., Ishida, S., Imai, Y., Watanabe, Y., and Wada, S., 2020, "Multiscale modeling of human cerebrovasculature: A hybrid approach using image-based geometry and a mathematical algorithm", *PLoS Comput Biol*, Vol. 16 (6), p. e1007943.

[9] Kobayashi, M., Hoshina, K., Yamamoto, S., Nemoto, Y., Akai, T., Shigematsu, K., Watanabe, T., and Ohshima, M., 2015, "Development of an image-based modeling system to investigate evolutional geometric changes of a stent graft in an abdominal aortic aneurysm", *Circulation Journal*, Vol. 79, pp. 1534–1541.

[10] Yamada, S., Kobayashi, M., Watanabe, Y., Miyake, H., and Oshima, M., 2014, "Quantitative measurement of blood flow volume in the major intracranial arteries by using 123I-iodoamphetamine SPECT", *Clinical Nuclear Medicine*, Vol. 39 (10), pp. 868–873.

[11] Perlmutter, D., and Rhoton, A. L. J., 1978, "Microsurgical anatomy of the distal anterior cerebral artery", *Journal of Neurosurgery*, Vol. 49 (2), pp. 204–228.

[12] Gibo, H., Carver, C. C., Rhoton, A. L. J., Lenkey, C., and Mitchell, R. J., 1981, "Microsurgical anatomy of the middle cerebral artery", *Journal of Neurosurgery*, Vol. 54 (2), pp. 151–169.

[13] Zeal, A. A., and Rhoton, A. L. J., 1978, "Microsurgical anatomy of the posterior cerebral artery", *Journal of Neurosurgery*, Vol. 48 (4), pp. 534–559.

[14] Hoefer, I. E., van Royen, N., Buschmann, I. R., Piek, J. J., and Schaper, W., 2001, "Time course of arteriogenesis following femoral artery occlusion in the rabbit", *Cardiovascular Research*, Vol. 49 (3), pp. 609–617.

[15] Cheng, H., Chen, X., Zhong, J., Li, J., Qiu, P., and Wang, K., 2022, "Label-free measurement of wall shear stress in the brain venule and arteriole using dual-wavelength third-harmonic-generation line-scanning imaging", *Optics Letters*, Vol. 47 (21), pp. 5618–5621.

[16] Yamada, S., Otani, T., Ii, S., Ito, H., Iseki, C., Tanikawa, M., Watanabe, Y., Wada, S., Oshima, M., and Mase, M., 2024, "Modeling cerebrospinal fluid dynamics across the entire intracranial space through integration of four-dimensional flow and intravoxel incoherent motion magnetic resonance imaging", *Fluids and Barriers of the CNS*, Vol. 21 (1), p. 47.